Revised manuscript with yellow highlight

Flash healing of Vickers microcracks formed on the (001) surface of cubic zirconia single crystals

Shunsuke KAYUKAWA[a], Yutaro KATSUYAMA[a], Ayu KODAIRA[a], Tomoharu TOKUNAGA[a], Koji MORITA[b], Atsutomo NAKAMURA[c], and Takahisa YAMAMOTO[a,*]

[a]Department of Materials Design Innovation Engineering, Nagoya University, Furo-cho, Chikusa-ku, Nagoya, 464-8603, Japan

[b]Research Center for Functional Materials, National Institute for Materials Science, Sengen 1-2-1, Tsukuba, Ibaraki 305-0047, Japan

[c]Department of Mechanical Science and Bioengineering, Osaka University, 1-3 Machikaneyamacho, Toyonaka, Osaka 560-8531, Japan

Corresponding author: T. Yamamoto; E-mail: yamamoto.takahisa@material.nagoya-u.ac.jp

Keywords: flash healing, microcrack, zirconia, lattice diffusion, STEM

Abstract

Flash healing, a technique for microcrack healing using a flash event, has recently attracted attention for effective microcrack healing of ceramics. To investigate the diffusion-accelerated phenomena that occur during flash healing, the flash-healing behavior of Vickers indentation microcracks on (001) zirconia single crystals was investigated, mainly from the viewpoint of microstructure analysis of the healed microcracks. Scanning electron microscopy and atomic force microscopy showed that the surface microcracks were rapidly healed. However, scanning transmission electron microscopy showed that a row of pores remained along the original microcrack inside the crystal, and the crystallographic orientation relationship on both sides of the microcrack was restored to that of the original single crystal. Compared with the findings for healing without an electric field, the distance from the pore closest to the surface was larger and the total pore volume was smaller for flash healing. These results suggest that flash treatment increases lattice diffusion.

1. Introduction

Most ceramics fail owing to brittle fracture caused by crack propagation associated with microcrack growth under stress [1]. To prevent brittle fracture and increase the lifetime of ceramics, microcrack growth must be suppressed. Techniques to suppress microcrack growth by using phase transformation [2, 3] and composites [4, 5] have been reported. In contrast, techniques to repair the microcracks themselves have also been proposed, which is called microcrack healing [6, 7]. One of the simplest techniques to heal microcracks is the thermal healing technique using the diffusion process enhanced by annealing at high temperatures [8, 9].

Gupta [10,11] reported the microcrack healing process during thermal healing of alumina polycrystals from the viewpoint of microstructure analysis. He suggested that microcrack healing precedes as follows: the inner surfaces of the microcracks contact each other, the contact point area increases to form cylindrical voids, the cylindrical voids break up and are isolated mainly by surface diffusion, and the isolated voids shrink and disappear by grain boundary and lattice diffusion. Each of these processes is facilitated by increasing mass diffusion. Recently, flash healing using the flash event that occurs when an electric field is applied has been proposed to enhance the microcrack healing process [12,13]. The flash event is the occurrence of an electric power spike when oxide ceramics are heated under an appropriate electric field [14–16]. Large-scale mass diffusion is induced by the instantaneous electric power spike with the flash event [17–20]. For example, in flash sintering, which uses this flash event for a sintering process, stabilized zirconia ceramics can be densified in only a few seconds at a furnace temperature of approximately 850 °C [21]. Morita et al. applied this flash event to healing of Vickers indentation microcracks in zirconia polycrystals [12]. They found that microcracks of approximately 20 μm in length were completely healed after approximately 10 min of flash treatment at a sample temperature of approximately 1230 °C. Takahashi et al. [22] revealed the relationship between the grain size and the microcrack

healing behavior [22]. They found that as the grain size increases, microcracks are less likely to be repaired. Their results suggest the importance of grain boundary diffusion in the microcrack healing process. Similar experiments using single crystals without grain boundaries are required to clarify the effect of grain boundaries on the microcrack healing process by flash treatment.

In this study, we used a single crystal of ZrO_2 doped with 10 mol% Y_2O_3 as a model material and performed microstructural analysis of the flash-healed microcracks formed by Vickers indentation, mainly by scanning transmission electron microscopy (STEM). The experimental conditions, such as the initial microcrack length and sample temperature, were set to be as consistent as possible with the conditions used for microcrack healing of zirconia polycrystals [12,22].

2. Materials and Methods

Commercially available cubic zirconia single crystals (10 mol% Y_2O_3–ZrO_2; Shinkosha Co., Ltd. , Japan) with dimensions of 0.5 mm × 10 mm × 10 mm were used. The large 10 mm × 10 mm surface was the (001) plane mirror-finished by the manufacturer. The samples used for flash healing were machined from this single crystal and had dimensions of 0.5 mm × 2 mm × 10 mm. The microcracks were generated on the (001) surface by the indentation method using a micro-Vickers indenter (Via-S, Matsuzawa Co., Ltd.) at a load of 100 gf applied for 15 s, as schematically shown in Fig. 1. The Vickers indents was formed so that its edges were parallel to (010) and (100). Microcracks are expected to form along the [110] and [1$\bar{1}$0] directions vertical to the (001) single-crystal surface by Vickers indentation in this direction [23].

After indentation, the samples were flash healed using direct current (DC) and alternative current (AC) electric fields. The samples with indents were set in a high-temperature dilatometer (EVO2 TMA8311, Rigaku, Japan) modified to apply an electric field [24]. Platinum sheets were used as the electrodes on both longitudinal faces of the samples, and no Pt paste was used. The samples were furnace-heated at a heating rate of 5 °C/min under application of electric fields using a power supply (Asterion AST-751, AMETEK.com) that was initially set in voltage-control mode. The electric fields were set at 100 V/cm with a limit current of 150 or 350 mA/cm^2 for the DC electric field, and at 100 V/cm (a root-mean-square value) with a limit current of 350 mA/cm^2 (a root-mean-square value) for the AC electric field. After the flash event occurred, the furnace temperature was kept constant for 10 min under the electric field. The power supply and furnace were then switched off and the samples were furnace-cooled to room temperature. The time for cooling to room temperature was approximately 20 min.

The surface morphology and topology in the vicinity of the indents were observed by scanning electron microscopy (SEM; MI4000L, Hitachi High-Tech Corp.) under a low acceleration voltage of 1 kV to increase the surface sensitivity, confocal optical microscopy (OPTELICS

HYBRID +, Lasertec Corp.), and atomic force microscopy (AFM; JSPM-4210, JEOL, Ltd.) using a SSS-NCLR-20 cantilever (Nano World AG, Ltd.) in non-contact mode in the ambient atmosphere at room temperature. The microstructure along a healed microcrack inside the single crystal was observed by STEM (ARM-200FC, JEOL Ltd.) at an acceleration voltage of 200 kV. For STEM imaging, STEM thin foils were prepared using a focused ion beam (FIB, ETHOS NX5000, Hitachi High-Tech Corp.). FIB pick-up was conducted to let STEM observation direction parallel to the original microcrack plane (the details are shown in Fig. 1). The thickness of the STEM thin foils was adjusted to approximately 60 nm during the FIB process, which is a similar thickness to that in our previous report describing thermal healing of Vickers-indented microcracks without an electric field [25].

3. Results

The changes of the electric power dissipation and sample temperature with the process time during flash healing are shown in Fig. 2(a) and (b), respectively. The flash temperatures are indicated in Fig. 2(a). For all of the samples, the electric current and furnace temperature were held constant for 10 min after the power spike occurred at the specific flash temperature. The flash temperature (T_F) was approximately 740 °C for the DC electric fields and 630 °C for the AC electric field. Although the initial electric fields were the same, there was a slight decrease in the flash temperature for the AC electric field. After the occurrence of the power spike, the power dissipation asymptotically approached a roughly constant value. From an equation based on a black-body radiation model [26], the sample temperatures between 1 and 10 min after the flash event occurred were roughly calculated to be 1250 °C for the DC 150 mA/cm^2 sample, 1400 °C for the DC 350 mA/cm^2 sample, and 1350 °C for the AC 350 mA/cm^2 sample, respectively. Hereafter, these samples are referred to as the DC-1250°C, DC-1400°C, and AC-1350°C samples.

SEM images of the areas including the Vickers indents and the height profiles obtained along the white lines indicated in the respective SEM images are shown in Fig. 3(a)–(d) and 3(e)–(h), respectively. The height profiles were measured by confocal microscopy. In the pristine sample (Fig. 3(a)), a square-shaped indent formed with sides along the [100] and [010] directions, and microcracks formed along the [110] and [$1\bar{1}0$] directions from the respective vertexes of the indent, as expected [23]. The distance from the indent center at the surface to the bottom of the microcrack was approximately 1.1 μm (Fig. 3(e)). The average length of the diagonal dimensions of the indent was approximately 11.7 μm, and the average half-length of the microcrack measured from the center of the indent was approximately 22.5 μm.

The surface morphology greatly changed after flash healing (Fig. 3(b)–(d)). Material uplift occurred around the indent in the DC-1250°C sample. Owing to this material uplift, the indent depth became slightly smaller than that of the pristine sample as presented in height profile of

(f). The microcracks on the surface were healed, but the surface was slightly concave along the original microcracks near the indent vertexes. In the DC-1400°C sample, distinct facets formed on the surface around the indent and also on the indent inner surface, which were mostly along the [110] and [$1\bar{1}0$] directions. The slight concavity along the original microcracks observed in the DC-1250°C sample was not observed in the DC-1400°C sample. The microcracks on the surface were completely healed. In the AC-1350°C sample, although the surface morphology around the indent was similar to that in the DC-1250°C sample, no surface concavity was observed along the original microcracks, as in the DC-1400°C sample.

Cross-sectional HAADF-STEM observations along the healed microcracks after flash healing are shown in Fig. 4, where each STEM image is shown with the indented (001) surface on the top. In all of the samples, the microcracks at/near the surface were healed, which is consistent with the SEM images (Fig. 3(b)–(d)). However, a large number of pores corresponding to the unhealed state were observed in the crystal interiors. These aligned pores are considered to be present along the original microcracks. The horizontal white arrows in Fig. 4(a)–(c) indicate the pores closest to the surface. The distance from the surface to the pore closest to the surface was approximately 40 nm in the DC-1250°C sample, 520 nm in the DC-1400°C sample, and 320 nm in the AC-1350°C sample. Healing of the microcracks near the surface region was more advanced in the DC-1400°C and AC-1350°C samples than in the DC-1250°C sample. The inserts in Fig. 4(a)–(c) show selected-area diffraction (SAD) patterns including both sides of the arrays of pores. Although microcrack healing was not perfectly completed, the crystals on both sides of the microcracks returned to their original single crystal orientation relationship, as shown in the respective SAD patterns. Higher magnification HAADF-STEM images of the pore arrays are shown in Fig. 4(d)–(f), confirming the characteristic pore shapes. In all of the samples, pores with a rhombus-like shape were observed (e.g., the black arrow in Fig. 4(e)). In addition, nearly hexagonal pores were observed in the AC-1350°C sample (e.g., the black arrow in Fig. 4(f)). These observations suggest that the pores were surrounded by specific inner

surfaces, presumably with low surface energy, which will be discussed later [25,27,28].

High-resolution HAADF-STEM images of a rhombic pore observed in the DC-1400°C sample and a hexagonal pore observed in the AC-1350°C sample, as typical examples, are shown in Fig. 5(a) and (b), respectively. The areas including the pores had the same crystal structures as the original single crystal, which is consistent with SAD patterns shown in Fig. 4(a)–(c). The side planes of the rhombic pore were {111} surfaces, while {001} surfaces appeared in addition to {111} surfaces for the hexagonal pore. As indicated by the white dashed box in Fig. 4(f), the edges of two pores partially overlapped vertically in the STEM thin foil, meaning that the thickness of these pores was less than approximately 60 nm (the thickness of the STEM thin foil). This suggests that these pores had plate-like shapes.

The temperature dependence of the healing ratio for the DC-1250°C, DC-1400°C, and AC-1350°C samples is shown in Fig. 6 (open red and blue symbols). The healing ratio was estimated in two ranges: in the near-surface region (1 μm from the surface, L = 1 μm) and in the interior region (from 1 μm from the surface to 4 μm, L = 3 μm), as shown in the schematic diagram in Fig. 6(a). The healing ratio δ is defined as the sum of the individual pore lengths ΔL_i contained within a length L along the original microcrack:

$$\delta = \frac{L - \sum_{i=1}^{i=m \text{ or } n} \Delta L_i}{L} \times 100\ (\%)$$

In the near-surface region (open circles), the healing ratio increased with increasing sample temperature. This is consistent with the result that the distance from the surface of the pore closest to the surface increased with increasing sample temperature (Fig. 4(d)–(f)). In contrast, the healing ratio was approximately constant regardless of the sample temperature in the interior region (open squares). In other words, the total volume of the pores in the near-surface region decreased with increasing sample temperature, but that of the pores in the interior region did not change. Previous data obtained for microcrack healing by heat treatment without applying an electric field (black plus signs) and the values reported for zirconia polycrystals by

Takahashi et al. [22] (green solid triangles) are also shown in Fig. 6. These data will be discussed later.

Surface topological images of the DC-1400°C and AC-1350°C samples obtained by AFM and the height profiles along the black lines indicated in the AFM images are shown in Fig. 7. In the AFM image of DC-1400°C (Fig. 7(a)), the direction of the DC electric field is indicated by a black block arrow. In the SEM image of DC-1400°C (Fig. 3(c)), the facets on the surface of the DC-1400°C sample mostly formed along the [110] and [$1\bar{1}0$] directions. This facet structure was clearly observed in the AFM topographic image of DC-1400°C (Fig. 7(a)). From the AFM image, the facet structure observed as lines in the SEM image corresponds to the edges of the material uplift from the surface. As shown in the height profile taken along the black line indicated in Fig. 7(a), the material uplift had a saw-like shape with a height of approximately 40 nm (Fig. 7(c)). The height profile showed that the slope of the side wall of this material uplift was asymmetric along the direction of the electric field (from A to B in Fig. 7(a)), with a smaller slope on the front side, as indicated by the arrow in Fig. 7(c). In contrast, the surface of the AC-1350°C sample (Fig. 7(b)) did not show the material uplift observed in the DC-1400°C sample (Fig. 7(a)). In this case, surface step-like structures with heights of approximately 0.2–0.4 nm formed, and some step bunching due to destabilization of the step lines was also observed, as indicated by the black arrows in Fig. 7(b). The large-scale material uplift observed in the DC-1400°C sample is due to drift diffusion by a unidirectional electric field [29, 30].

4. DISCUSSION

4.1. Pore annihilation and field-applied effects for lattice diffusion

After flash healing, the microcrack at the surface was healed with pores remaining in the crystal interior, and the crystal orientation on both sides of the original microcrack was restored to the same orientation relationship as that of the original single crystal. The residual pores were rhombus shaped surrounded by {111} surfaces or hexagon shaped surrounded by {111} and {001} surfaces, in which the upper/lower surfaces of both shapes were possibly surrounded by {110} surfaces. These surrounding inner surfaces are planes with relatively low surface energy [27,28] as discussed previously [25]. The microstructural features observed in the flash-healed single crystals were similar to the results obtained in our previous study on microcrack healing by annealing without an electric field, as shown in Fig. S1 [25]. However, in the case of flash healing, the location of the pore present at the surface-nearest-neighbor position was significantly different from that with no-electric-field thermal healing. In no-electric-field thermal healing, the pore inside the crystal remained close to the surface in the thermal healed sample, in which the distance from the surface to the pore present at the surface-nearest-neighbor position was approximately 40 nm irrespective of the annealing temperature (Fig. S1). In contrast, in the sample after flash healing, the surface-nearest-neighbor pores were located further inside the crystal, as shown in Fig. 4(b) and (c).

The above difference can be inferred to be related to the increase in lattice diffusion during flash treatment as follows. Because the crystallographic orientation relationship is restored to that of the single crystal during flash healing, pore annihilation proceeds by mass diffusion through lattice diffusion. For a pore to be annihilated, the volume contained in the pore must diffuse to the surface through lattice diffusion. The distance from the surface to the pore closest to the surface d is an indication of the amount of mass diffusion through lattice diffusion during healing. As mentioned above, for the DC-1250°C sample, d was approximately 40 nm, which was comparable to the d values of thermal healed samples with no electric field (Fig. S1). In

contrast, for the DC-1400°C sample, *d* was approximately 520 nm. This suggests that lattice diffusion increased in the DC-1400°C sample compared with that in the DC-1250°C sample. This increase in lattice diffusion induced by the electric field during flash healing can be considered to be responsible for the increased healing ratio in the near-surface region, as shown in Fig. 6(b) (open circles).

For pores located in the region at a larger distance than *d*, the total volume of the pores hardly changes because it is beyond the distance that pores can be eliminated by lattice diffusion. This was confirmed by the total volume of the pores present in this region hardly changing with the sample temperature, as shown in Fig. 6(b) (open rectangles). In this region, the pore diameter variation due to Ostwald ripening becomes remarkable, in which pores with large diameters become larger, while those with small diameters disappear. This pore size variation due to Ostwald ripening can be observed in the pore size difference by comparing Fig. 4(d) and 4(e), in which the difference in the pore diameter increased for the DC-1400°C sample. The situation in which pores located greater than *d* from the surface are difficult to eliminate should be the same regardless of flash or thermal healing. In fact, the healing ratio in the crystal interior by thermal healing does not change with the sample temperature (plus signs in Fig. 6(b)) [25]. However, the value of *d* will increase if the temperature and time are sufficient to promote lattice diffusion even in thermal healing. Similarly, *d* is expected to increase further also in flash healing.

According to Gupta [10,11], in the early stage of microcrack healing, there is a progressive increase in the contact area between the crack inner surfaces owing to surface diffusion. As shown in Fig. 7, the DC-1400°C sample showed surface material uplift with a height of approximately 40 nm and the characteristic facet structure. This surface material uplift is considered to be due to drift diffusion induced by the DC electric field [29,30]. In contrast, the AC-1350°C sample did not show the effect of drift diffusion that occurred during application of the DC electric field, and no facet structure was observed on the crystal surface. This

difference in the surface morphologies under DC and AC electric fields indicates a difference in surface diffusion, which is expected to affect the early stage of healing. However, from the healing ratios (Fig. 6), the healing ratio in the AC-1350°C sample was close to the sample temperature dependence of the healing ratios of the DC-1250°C and DC-1400°C samples. This means that the contribution of surface diffusion to the early stages of microcrack healing is possibly not significant for zirconia single crystals.

4.2. Role of grain boundaries during flash healing

As mentioned above, once a pore is isolated and confined within the crystal interior that has been restored to the single crystal orientation relationship during microcrack healing, a subsequent decrease in the total volume of the pores is very unlikely to occur. To increase the annihilation rate, more effective diffusion paths are necessary, and grain boundaries act as effective diffusion paths for this purpose. Morita and co-workers [12, 22] systematically investigated the flash-healing behavior of microcracks in zirconia polycrystals. The results of flash healing of microcracks in zirconia polycrystals with different grain sizes, that were flash treated with DC electric field, are shown as green solid triangles in Fig. 6 [22]. In the case of a zirconia polycrystal with a grain size of approximately 0.8 μm, the microcrack was completely healed in 10 min by DC flash healing at a sample temperature of 1230 °C. Healing of microcracks in the zirconia polycrystals was confirmed to be completed not only on the surface, but also in the interior. This healing ratio is much higher than those obtained for zirconia single crystals. This means that grain boundaries allow healing to rapidly proceed. The healing ratio significantly decreased as the grain size of the zirconia polycrystal increased. This is probably because a larger distance must be travelled via lattice diffusion for larger grain size. This situation is similar to the discussion of the positional relationship of the surface-nearest pore to the surface described in Section 4.1. In other words, the reason why the healing ratio decreases with increasing grain size is probably the existence of grain boundaries located at a distance

greater than the distance at which pores can be annihilated. Grain boundaries act as effective annihilation sites for pores contained in grain interiors [31]. Nambu et al. [32] observed similar annihilation of pores in the presence of grain boundaries by flash bonding. Thus, the presence of grain boundaries may play an important role in promoting flash repair.

5. Conclusions

Microstructural observations, mainly by STEM, have been performed for flash-healed microcracks formed by a Vickers indentation on the (001) surface of cubic zirconia single crystals. The following results were obtained.

(1) The microcracks on the (001) plane of the single crystal due to Vickers indentation formed along the [110] and [$1\bar{1}0$] directions with an average half-length from the center of the indent of approximately 22.5 μm.

(2) Surface observation by SEM revealed that the surface area where the microcracks existed was healed by flash healing for 10 min at 100 V/cm with limit currents of 150 and 350 mA/cm^2 for a DC electric field, and at 100 V/cm with a limit of 350 mA/cm^2 for an AC electric field.

(3) Internal observation by STEM revealed that the crystallographic orientation of the crystal areas containing a closed microcrack completely returned to that of the original single crystal, although a row of plate-like rhombic and hexagonal pores remained along the original microcrack location. Elimination of these pores can be considered to proceed by lattice diffusion.

(4) The healing ratio of the near-surface region by flash healing was higher than that by thermal healing without an electric field. Furthermore, the location of the pore closest to the surface was further inside the crystal for flash healing than for thermal healing. These results suggest that lattice diffusion is enhanced by flash healing.

(5) Pores located in the interior of the crystal beyond the distance that can be eliminated by lattice diffusion are difficult to eliminate. The presence of grain boundaries with fast diffusion paths beyond the distance that can be eliminated by flash treatment is effective to eliminate these pores.

Acknowledgments

This work was financially supported by CREST (JPMJCR1996) from the Japan Science and Technology Agency, and JSPS KAKENHI (Grant Number JP19H05788).

References

1) A. G. Evans, Perspective on the development of high-toughness ceramics, J. Am. Ceram. Soc., 73 (1990) 187-206. https://doi:10.1111/j.1151-2916.1990.tb06493.x

2) R. C. Garvie, R.H. Hannink, Ceramic steel?, Nature, 258 (1975) 703–704. https://doi:10.1038/258703a0.

3) J. Wang, R. Stevens, Zirconia-toughened alumina (ZTA) ceramics, J. Mater. Sci., 24 (1989) 3421–3440. https://doi:10.1007/BF02385721.

4) H. Siddiqui, K. Pickering, M. Mucalo, A review on the use of hydroxyapatite-carbonaceous structure composites in bone replacement materials for strengthening purposes, Materials, 11 (2018) 1813. https://doi:10.3390/ma11101813.

5) S. Gali, K.R. Kumar, B.V.S. Murthy, B. Basu, Zirconia toughened mica glass ceramics for dental restorations, Dental Mater., 34 (2018) e36–e45. https://doi:10.1016/j.dental.2018.01.009.

6) I. Hammood, G. Barber, B. Wang, A review of some of experimental and numerical studies of self-crack-healing in ceramics, Int. J. Ceram. Eng. Sci., 2 (2020) 274–291. https://doi.org/10.1002/ces2.10071

7) F. Tavangarian, D. Hui, G. Li, Crack-healing in ceramics, Compos. B. Eng., 144 (2018) 56–87. https://doi.org/10.1016/j.compositesb.2018.02.025

8) FF. Lange, KC Radford, Healing of surface cracks in polycrystalline Al_2O_3, J. Am. Ceram. Soc., 53 (1970) 420–421. https://doi.org/10.1111/j.1151-2916.1970.tb12148.x

9) FF. Lange, TK. Gupta TK. Crack healing by heat treatment. J. Am. Ceram. Soc., 53 (1970) 54–55. https://doi.org/10.1111/j.1151-2916.1970.tb12002.x

10) T.K. Gupta, Instability of cylindrical voids in alumina, J. Am. Ceram. Soc., 61 (1978) 191-195. https://doi.org/10.1111/j.1151-2916.1978.tb09276.x

11) T.K. Gupta, Crack healing and strengthening of thermally shocked alumina, J. Am. Ceram. Soc., 59 (1976) 259-262. https://doi.org/10.1111/j.1151-2916.1976.tb10949.x

12) K. Morita, F. Naito, D. Terada, Microcrack healing in zirconia ceramics under a DC electric

field/current, J. Eur. Ceram. Soc., 41 (2021) 282–289. https://doi.org/10.1016/j.jeurceramsoc.2021.09.044

13) J. Dong, V. M. Sglavo, M. Kermani, X. Su, T. Saunders, C. Hu, S. Grasso, Athermal electric field effects in flash sintered zirconia, Adv. Appl. Ceram., 120 (2021) 193-201. https://doi.org/10.1080/17436753.2021.1919361

14) M. Cologna, B. Rashkova, R. Raj, Flash sintering of nanograin zirconia in <5s at 850◦C, J. Am. Ceram. Soc., 93 (2010) 3556–3559. https://doi.org/10.1111/j.1551-2916.2010.04089.x

15) M. Yu, S. Grasso, R. Mckinnon, T. Saunders, M.J. Reece, Review of flash sintering: materials, mechanisms and modelling, Adv. Appl. Ceram., 116 (2017) 24–60. https://doi.org/10.1080/17436753.2016.1251051

16) O. Guillon, R.A. De Souza, T.P. Mishra, W. Rheinheimer, Electric‐field‐assisted processing of ceramics: nonthermal effects and related mechanisms, MRS Bull., 46 (2021) 52–58. https://doi.org/10.1557/s43577-020-00008-w

17) Y. Ishino, K. Taguchi, M. Koike, T. Tokunaga, T. Yamamoto, Shrinkage rate control during a flash state by current-ramping for 3 mol% Y_2O_3-doped ZrO_2 polycrystals, J. Am. Ceram. Soc., 104 (2021) 4960–4967. https://doi.org/10.1111/jace.17912

18) H. Yoshida, Y. Sakka, T. Yamamoto, JM. Lebrun, R. Raj, Densification behavior and microstructural development in undoped yttria prepared by flash-sintering, J. Euro. Ceram. Soc., 34 (2014) 991-1000. https://10.1016/j.jeurceramsoc.2013.10.031

19) R.I. Todd, E.Z. Solvas, R.S. Bonilla, T. Sneddon, P.R. Wilshaw, Electrical characteristics of flash sintering: thermal runaway of Joule heating, J. Euro. Ceram. Soc., 35 (2015) 1865-1877. https://10.1016/j.jeurceramsoc.2014.12.022.

20) K. Ren, QK. Wang, YL. Lian, YG. Wang, Densification kinetics of flash sintered 3mol% Y_2O_3 stabilized zirconia, J. Alloys Compd., 747 (2018) 1073-1077. https://10.1016/j.jallcom.2018.02.308

21) M. Cologna, A.L. Prette, R. Raj, Flash-sintering of cubic yttria-stabilized zirconia at 750 ℃

for possible use in SOFC manufacturing, J. Am. Ceram. Soc., 94 (2011) 316–319.

22) S. Takahashi, K. Morita, K. Nambu, D. Terada, K. Kobayashi, T. Tokunaga, T. Yamamoto, Effect of initial grain size on crack healing behavior under DC electric field of zirconia (8Y-CSZ) ceramic, Adv. Eng. Mater., (2023) 2201807. https://10.1002/adem.202201807.

23) A. Pajares, F. Guiberteau, A. D-Rodriguez, A. H. Heuer, Indentation-induced cracks and the toughness anisotropy of 9.4-mol%-yttria-stabilized cubic zirconia single crystals, J. Am. Ceram. Soc., 74 (1991) 859-862. https://doi.org/10.1111/j.1151-2916.1991.tb06941.x

24) N. Morisaki, H. Yoshida, K. Matsui, T. Tokunaga, K. Sasaki, T. Yamamoto, Synthesis of zirconium oxynitride in air under DC electric fields, Appl. Phys. Lett., 109 (2016) 083104. https://doi.org/10.1063/1.4961624

25) S. Kayukawa, Y Katsuyama, A. Kodaira, T. Tokunaga, K. Morita, A. Nakamura, K. Higuchi, T. Yamamoto, Microcrack healing in single-crystal cubic zirconia by thermal annealing, J. Euro. Ceram. Soc., 43 (2023) 1078–1086. https://doi.org/10.1016/j.jeurceramsoc.2022.10.065.

26) W.Ji, B. Parker, S.Falco, J.Y. Zhang, Z.Y. Fu, R.I.Todd, Ultra-fast firing: Effect of heating rate on sintering of 3YSZ, with and without an electric field, J. Euro. Ceram. Soc., 37 (2017) 2547-2551. http://dx.doi.org/10.1016/j.jeurceramsoc.2017.0.

27) A. Christensen, E.A. Carter, First-principles study of the surfaces of zirconia, Phys. Rev. B. 58 (1998) 8050–8064. https://doi.org/10.1103/PhysRevB.58.8050

28) G. Ballabio, M. Bernasconi, F. Pietrucci, S. Serra, Ab initio study of yttria-stabilized cubic zirconia surfaces, Phys. Rev. B., 70 (2004) 075417. https://doi.org/10.1103/PhysRevB.70.075417

29) Y. Homma, N. Aizawa, Electric-current-induced step bunching on Si (111), Phys. Rev. B., 62 (2000) 8323-8329. https://doi.org/10.1103/PhysRevB.62.8323

30) E. E. Rodyakina, S. S. Kosolobova, A.V. Latyshev, Drift of adatoms on the (111) silicon surface under electromigration conditions, JETP Lett., 94 (2011) 147–151.

https://doi.org/10.1134/S0021364011140128

31) J.E. Burke, Role of grain boundaries in sintering, J. Am. Ceram. Soc., 40 (1957) 80–85. https://doi.org/10.1111/j.1151-2916.1957.tb12580.x

32) K. Nambu, T. Kitaoka, K. Morita, K. Soga, T. Tokunaga, T. Yamamoto, H. Masuda, H. Yoshida, Flash self-joining of Y-TZP ceramics assisted with an AC electric field, J. Am. Ceram. Soc., 106 (2023) 2073-2082. https://doi.org/10.1111/jace.18889.

FIGURE 1

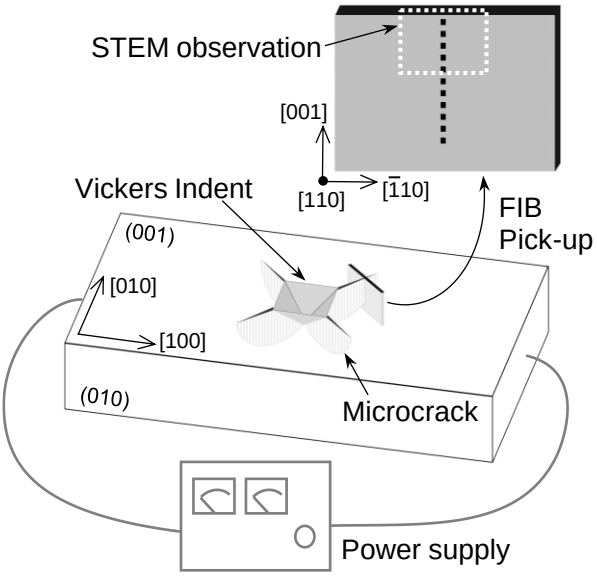

FIGURE 1

Schematic illustration of the sample setup for flash healing and FIB pick-up for STEM thin foil preparation with the crystallographic orientation index. The edges of Vickers indent are parallel to (010) and (100) of single crystal.

FIGURE 2

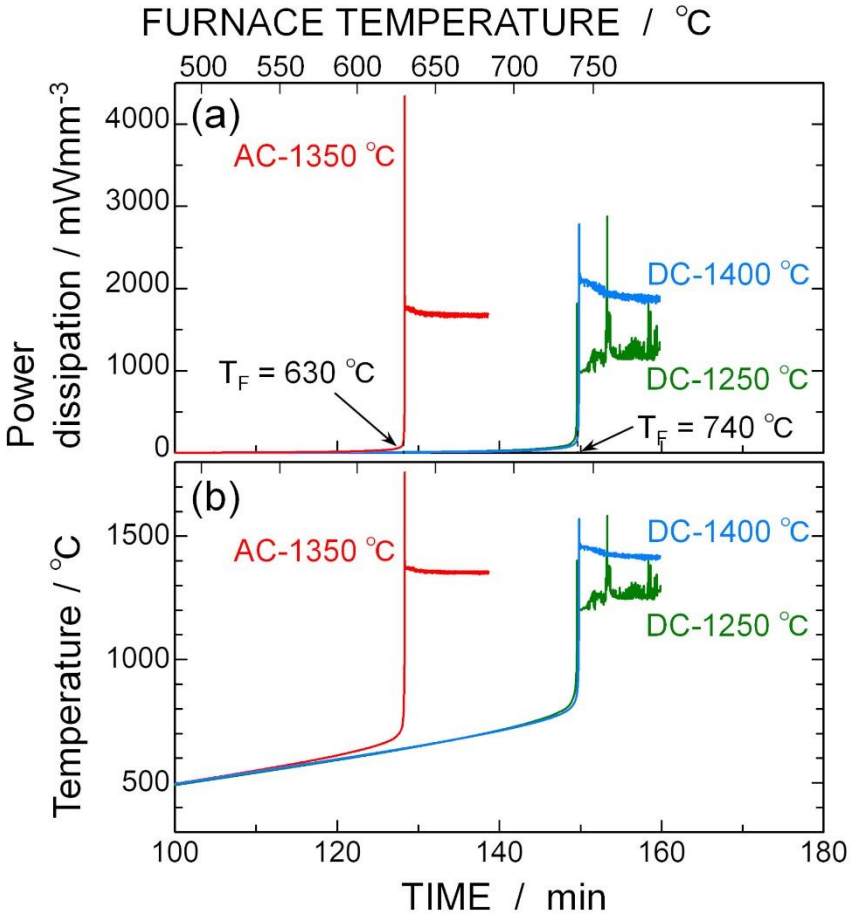

FIGURE 2

Changes of the (a) power dissipation and (b) sample temperature with the process time. The sample temperatures were calculated using an equation based on a black-body radiation model [26]. T_F is the flash temperature. Furnace temperature is indicated at an upper horizontal axis of (a) for reference. In respective flash treatment, when the furnace temperature reaches the respective flash temperature, the furnace temperature ramp is stopped and is maintained at a constant temperature thereafter.

FIGURE 3

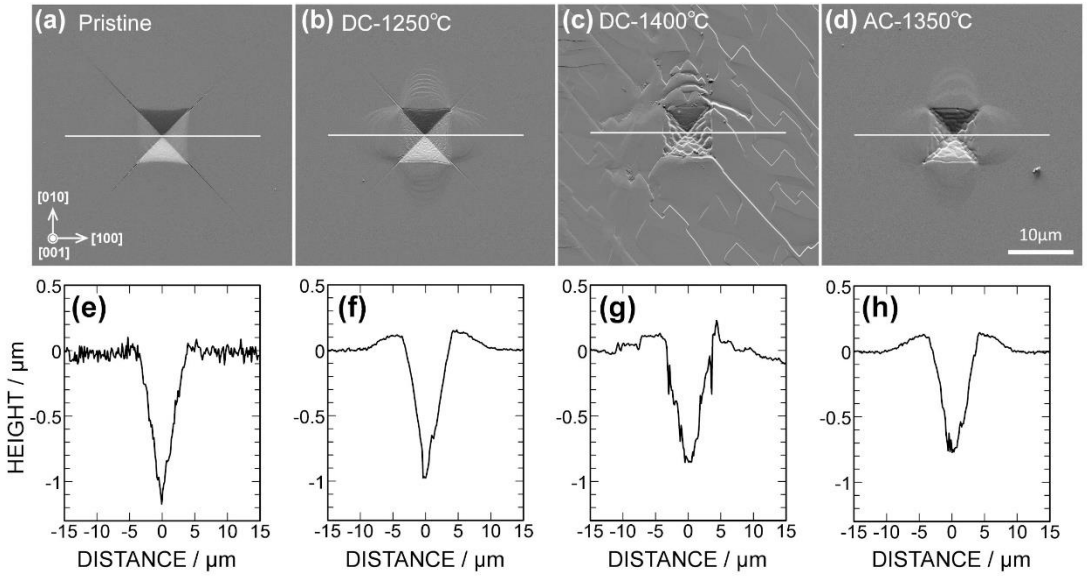

FIGURE 3

(a)–(d) SEM images of the surface morphologies and (e)–(h) height profiles as a function of the distance: (a) and (e) pristine sample, (b) and (f) DC-1250℃ sample, (c) and (g) DC-1400℃ sample, and (d) and (h) AC-1350℃ sample. The height profiles in (e)–(h) were taken along the white lines indicated in the respective SEM images. The label of the vertical axis of the height profiles is shown in (e). The SEM image and height profile of the pristine sample in (a) and (e) were taken from Ref. 25.

FIGURE 4

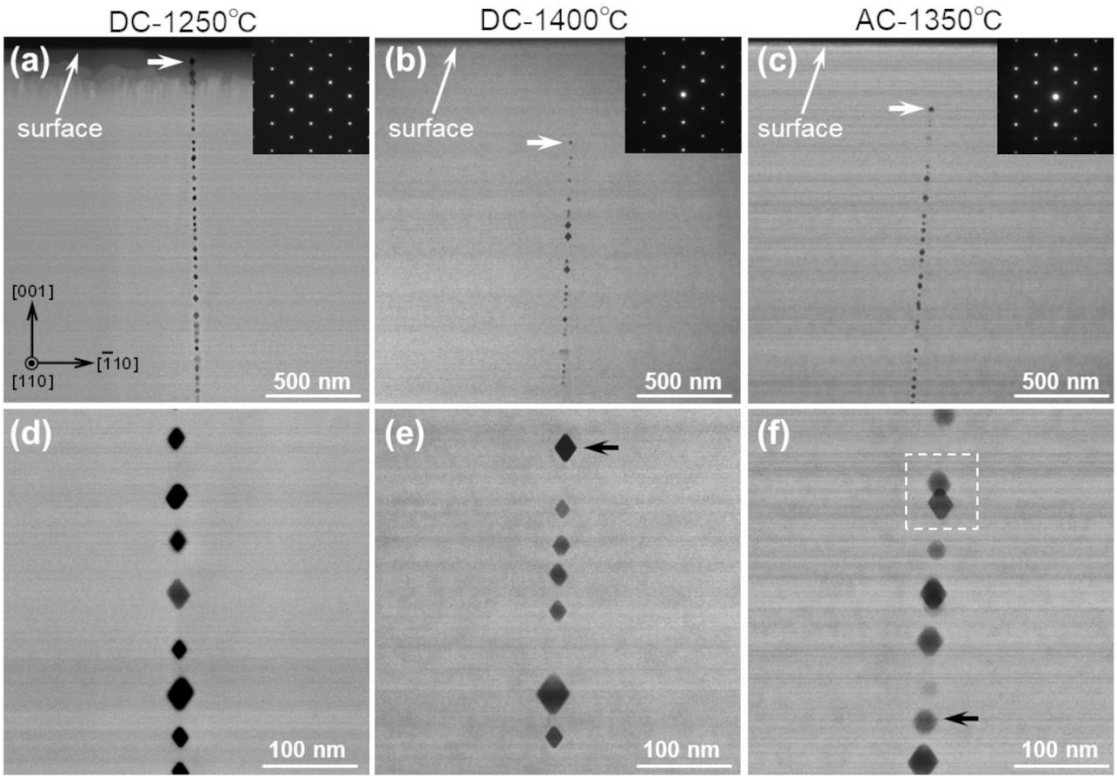

FIGURE 4

HAADF-STEM images of the (a) and (d) DC-1250 ℃, (b) and (e) DC-1400 ℃, and (c) and (f) AC-1350 ℃ samples. The horizontal white arrows in (a)–(c) indicate the pores closest to the surfaces. The inserts show the SAD patterns of the areas including both sides of the microcracks (rows of pores).

FIGURE 5

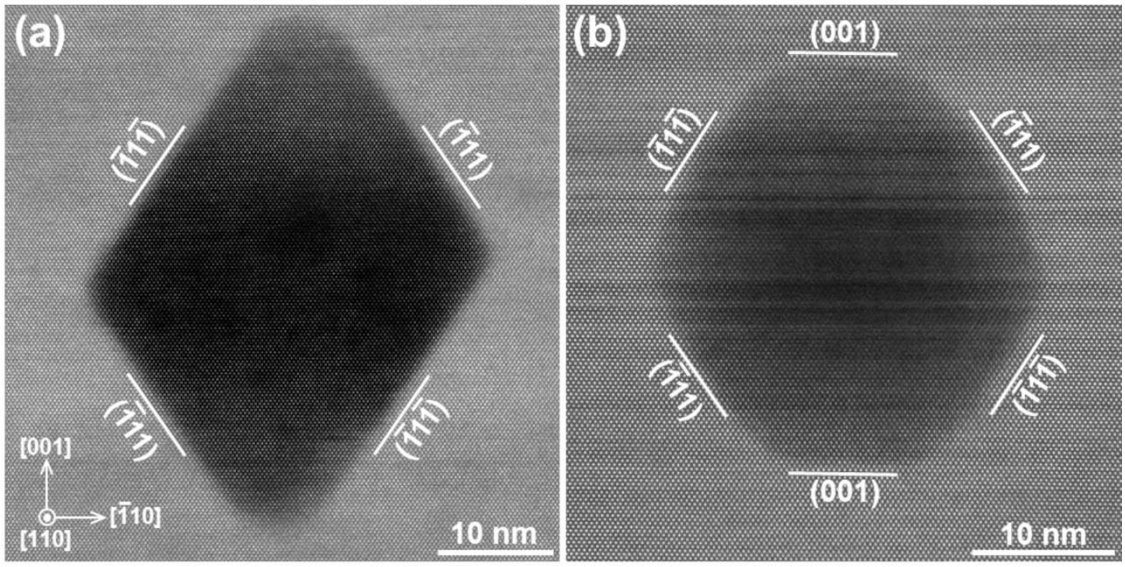

FIGURE 5

High resolution HAADF-STEM images of a typical rhombic pore in the DC-1400 ℃ sample and (b) a hexagonal pore in the AC-1350 ℃ sample. It is noted that scales of respective STEM images are different.

FIGURE 6

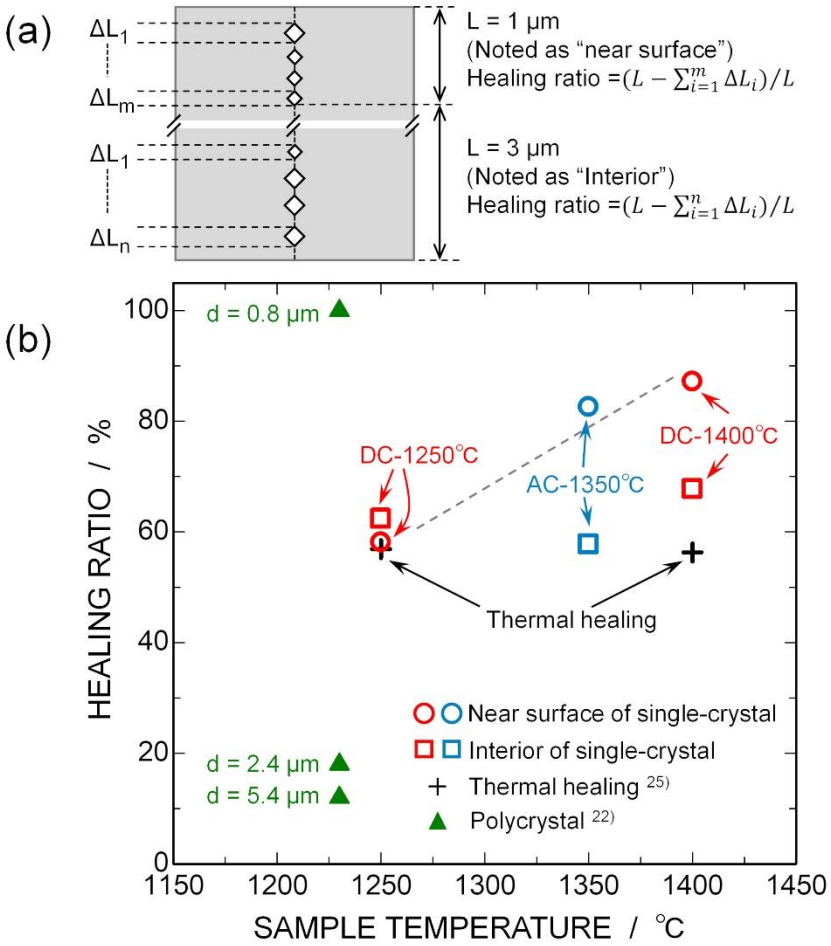

FIGURE 6

(a) Schematic illustration showing how the healing ratio was calculated. (b) Plot of the healing ratio against the sample temperature: ○, ○, near-surface region of the zirconia single crystals after flash healing; □, □, inside the zirconia single crystals after flash healing; **+**, after thermal healing of zirconia single crystals [25]; ▲, after flash healing of zirconia polycrystals [22]. The average grain sizes, *d*, of the polycrystals are indicated beside the ▲ symbols.

FIGURE 7

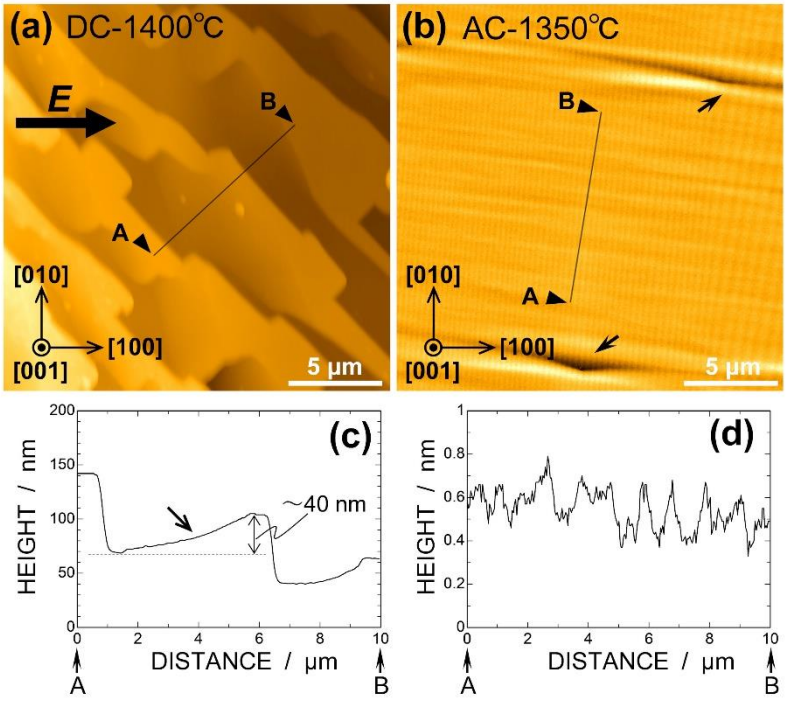

FIGURE 7

AFM topological images and height profiles along the black lines shown in the AFM images: (a) and (c) the DC-1400 ℃sample, and (b) and (d) the AC-1350 ℃sample. Note that the scales of the vertical axes of the height profiles are different.

Supplementary figure

FIGURE S1

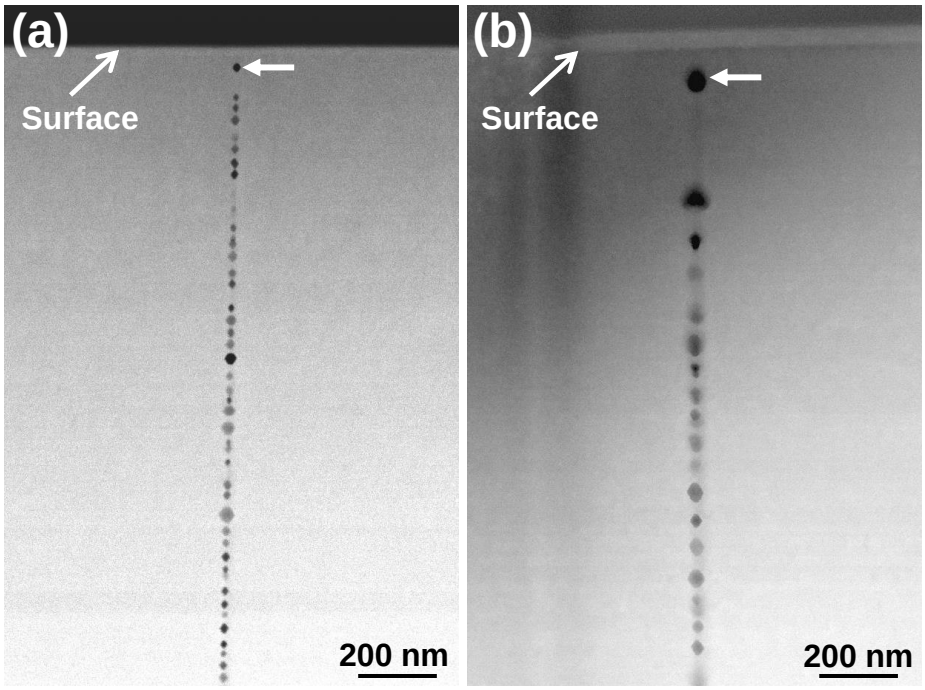

FIGURE S1

HAADF images taken from thermally healed cubic zirconia single crystals with Vickers indents that were annealed at (a) 1250 ℃, and (b) 1400 ℃. The block arrows show the pores closest to surfaces. These images were taken from Ref. 25.

Flash healing of Vickers microcracks formed on the (001) surface of cubic zirconia single crystals

Shunsuke KAYUKAWA[a], Yutaro KATSUYAMA[a], Ayu KODAIRA[a], Tomoharu TOKUNAGA[a], Koji MORITA[b], Atsutomo NAKAMURA[c], and Takahisa YAMAMOTO[a,*]

[a]Department of Materials Design Innovation Engineering, Nagoya University, Furo-cho, Chikusa-ku, Nagoya, 464-8603, Japan

[b]Research Center for Functional Materials, National Institute for Materials Science, Sengen 1-2-1, Tsukuba, Ibaraki 305-0047, Japan

[c]Department of Mechanical Science and Bioengineering, Osaka University, 1-3 Machikaneyamacho, Toyonaka, Osaka 560-8531, Japan

Corresponding author: T. Yamamoto; E-mail: yamamoto.takahisa@material.nagoya-u.ac.jp

Keywords: flash healing, microcrack, zirconia, lattice diffusion, STEM

Abstract

Flash healing, a technique for microcrack healing using a flash event, has recently attracted attention for effective microcrack healing of ceramics. To investigate the diffusion-accelerated phenomena that occur during flash healing, the flash-healing behavior of Vickers indentation microcracks on (001) zirconia single crystals was investigated, mainly from the viewpoint of microstructure analysis of the healed microcracks. Scanning electron microscopy and atomic force microscopy showed that the surface microcracks were rapidly healed. However, scanning transmission electron microscopy showed that a row of pores remained along the original microcrack inside the crystal, and the crystallographic orientation relationship on both sides of the microcrack was restored to that of the original single crystal. Compared with the findings for healing without an electric field, the distance from the pore closest to the surface was larger and the total pore volume was smaller for flash healing. These results suggest that flash treatment increases lattice diffusion.

1. Introduction

Most ceramics fail owing to brittle fracture caused by crack propagation associated with microcrack growth under stress [1]. To prevent brittle fracture and increase the lifetime of ceramics, microcrack growth must be suppressed. Techniques to suppress microcrack growth by using phase transformation [2, 3] and composites [4, 5] have been reported. In contrast, techniques to repair the microcracks themselves have also been proposed, which is called microcrack healing [6, 7]. One of the simplest techniques to heal microcracks is the thermal healing technique using the diffusion process enhanced by annealing at high temperatures [8, 9].

Gupta [10,11] reported the microcrack healing process during thermal healing of alumina polycrystals from the viewpoint of microstructure analysis. He suggested that microcrack healing precedes as follows: the inner surfaces of the microcracks contact each other, the contact point area increases to form cylindrical voids, the cylindrical voids break up and are isolated mainly by surface diffusion, and the isolated voids shrink and disappear by grain boundary and lattice diffusion. Each of these processes is facilitated by increasing mass diffusion. Recently, flash healing using the flash event that occurs when an electric field is applied has been proposed to enhance the microcrack healing process [12,13]. The flash event is the occurrence of an electric power spike when oxide ceramics are heated under an appropriate electric field [14–16]. Large-scale mass diffusion is induced by the instantaneous electric power spike with the flash event [17–20]. For example, in flash sintering, which uses this flash event for a sintering process, stabilized zirconia ceramics can be densified in only a few seconds at a furnace temperature of approximately 850 °C [21]. Morita et al. applied this flash event to healing of Vickers indentation microcracks in zirconia polycrystals [12]. They found that microcracks of approximately 20 μm in length were completely healed after approximately 10 min of flash treatment at a sample temperature of approximately 1230 °C. Takahashi et al. [22]

revealed the relationship between the grain size and the microcrack healing behavior [22]. They found that as the grain size increases, microcracks are less likely to be repaired. Their results suggest the importance of grain boundary diffusion in the microcrack healing process. Similar experiments using single crystals without grain boundaries are required to clarify the effect of grain boundaries on the microcrack healing process by flash treatment.

In this study, we used a single crystal of ZrO_2 doped with 10 mol% Y_2O_3 as a model material and performed microstructural analysis of the flash-healed microcracks formed by Vickers indentation, mainly by scanning transmission electron microscopy (STEM). The experimental conditions, such as the initial microcrack length and sample temperature, were set to be as consistent as possible with the conditions used for microcrack healing of zirconia polycrystals [12,22].

2. Materials and Methods

Commercially available cubic zirconia single crystals (10 mol% Y_2O_3–ZrO_2; Shinkosha Co., Ltd. , Japan) with dimensions of 0.5 mm × 10 mm × 10 mm were used. The large 10 mm × 10 mm surface was the (001) plane mirror-finished by the manufacturer. The samples used for flash healing were machined from this single crystal and had dimensions of 0.5 mm × 2 mm × 10 mm. The microcracks were generated on the (001) surface by the indentation method using a micro-Vickers indenter (Via-S, Matsuzawa Co., Ltd.) at a load of 100 gf applied for 15 s, as schematically shown in Fig. 1. The Vickers indents was formed so that its edges were parallel to (010) and (100). Microcracks are expected to form along the [110] and $[1\bar{1}0]$ directions vertical to the (001) single-crystal surface by Vickers indentation in this direction [23].

After indentation, the samples were flash healed using direct current (DC) and alternative current (AC) electric fields. The samples with indents were set in a high-temperature dilatometer (EVO2 TMA8311, Rigaku, Japan) modified to apply an electric field [24]. Platinum sheets were used as the electrodes on both longitudinal faces of the samples, and no Pt paste was used. The samples were furnace-heated at a heating rate of 5 °C/min under application of electric fields using a power supply (Asterion AST-751, AMETEK.com) that was initially set in voltage-control mode. The electric fields were set at 100 V/cm with a limit current of 150 or 350 mA/cm^2 for the DC electric field, and at 100 V/cm (a root-mean-square value) with a limit current of 350 mA/cm^2 (a root-mean-square value) for the AC electric field. After the flash event occurred, the furnace temperature was kept constant for 10 min under the electric field. The power supply and furnace were then switched off and the samples were furnace-cooled to room temperature. The time for cooling to room temperature was approximately 20 min.

The surface morphology and topology in the vicinity of the indents were observed by scanning electron microscopy (SEM; MI4000L, Hitachi High-Tech Corp.) under a low acceleration

voltage of 1 kV to increase the surface sensitivity, confocal optical microscopy (OPTELICS HYBRID +, Lasertec Corp.), and atomic force microscopy (AFM; JSPM-4210, JEOL, Ltd.) using a SSS-NCLR-20 cantilever (Nano World AG, Ltd.) in non-contact mode in the ambient atmosphere at room temperature. The microstructure along a healed microcrack inside the single crystal was observed by STEM (ARM-200FC, JEOL Ltd.) at an acceleration voltage of 200 kV. For STEM imaging, STEM thin foils were prepared using a focused ion beam (FIB, ETHOS NX5000, Hitachi High-Tech Corp.). FIB pick-up was conducted to let STEM observation direction parallel to the original microcrack plane (the details are shown in Fig. 1). The thickness of the STEM thin foils was adjusted to approximately 60 nm during the FIB process, which is a similar thickness to that in our previous report describing thermal healing of Vickers-indented microcracks without an electric field [25].

3. Results

The changes of the electric power dissipation and sample temperature with the process time during flash healing are shown in Fig. 2(a) and (b), respectively. The flash temperatures are indicated in Fig. 2(a). For all of the samples, the electric current and furnace temperature were held constant for 10 min after the power spike occurred at the specific flash temperature. The flash temperature (T_F) was approximately 740 °C for the DC electric fields and 630 °C for the AC electric field. Although the initial electric fields were the same, there was a slight decrease in the flash temperature for the AC electric field. After the occurrence of the power spike, the power dissipation asymptotically approached a roughly constant value. From an equation based on a black-body radiation model [26], the sample temperatures between 1 and 10 min after the flash event occurred were roughly calculated to be 1250 °C for the DC 150 mA/cm^2 sample, 1400 °C for the DC 350 mA/cm^2 sample, and 1350 °C for the AC 350 mA/cm^2 sample, respectively. Hereafter, these samples are referred to as the DC-1250°C, DC-1400°C, and AC-1350°C samples.

SEM images of the areas including the Vickers indents and the height profiles obtained along the white lines indicated in the respective SEM images are shown in Fig. 3(a)–(d) and 3(e)–(h), respectively. The height profiles were measured by confocal microscopy. In the pristine sample (Fig. 3(a)), a square-shaped indent formed with sides along the [100] and [010] directions, and microcracks formed along the [110] and [$1\bar{1}0$] directions from the respective vertexes of the indent, as expected [23]. The distance from the indent center at the surface to the bottom of the microcrack was approximately 1.1 μm (Fig. 3(e)). The average length of the diagonal dimensions of the indent was approximately 11.7 μm, and the average half-length of the microcrack measured from the center of the indent was approximately 22.5 μm.

The surface morphology greatly changed after flash healing (Fig. 3(b)–(d)). Material uplift

occurred around the indent in the DC-1250°C sample. Owing to this material uplift, the indent depth became slightly smaller than that of the pristine sample as presented in height profile of (f). The microcracks on the surface were healed, but the surface was slightly concave along the original microcracks near the indent vertexes. In the DC-1400°C sample, distinct facets formed on the surface around the indent and also on the indent inner surface, which were mostly along the [110] and [$1\bar{1}0$] directions. The slight concavity along the original microcracks observed in the DC-1250°C sample was not observed in the DC-1400°C sample. The microcracks on the surface were completely healed. In the AC-1350°C sample, although the surface morphology around the indent was similar to that in the DC-1250°C sample, no surface concavity was observed along the original microcracks, as in the DC-1400°C sample.

Cross-sectional HAADF-STEM observations along the healed microcracks after flash healing are shown in Fig. 4, where each STEM image is shown with the indented (001) surface on the top. In all of the samples, the microcracks at/near the surface were healed, which is consistent with the SEM images (Fig. 3(b)–(d)). However, a large number of pores corresponding to the unhealed state were observed in the crystal interiors. These aligned pores are considered to be present along the original microcracks. The horizontal white arrows in Fig. 4(a)–(c) indicate the pores closest to the surface. The distance from the surface to the pore closest to the surface was approximately 40 nm in the DC-1250°C sample, 520 nm in the DC-1400°C sample, and 320 nm in the AC-1350°C sample. Healing of the microcracks near the surface region was more advanced in the DC-1400°C and AC-1350°C samples than in the DC-1250°C sample. The inserts in Fig. 4(a)–(c) show selected-area diffraction (SAD) patterns including both sides of the arrays of pores. Although microcrack healing was not perfectly completed, the crystals on both sides of the microcracks returned to their original single crystal orientation relationship, as shown in the respective SAD patterns. Higher magnification HAADF-STEM images of the

pore arrays are shown in Fig. 4(d)–(f), confirming the characteristic pore shapes. In all of the samples, pores with a rhombus-like shape were observed (e.g., the black arrow in Fig. 4(e)). In addition, nearly hexagonal pores were observed in the AC-1350°C sample (e.g., the black arrow in Fig. 4(f)). These observations suggest that the pores were surrounded by specific inner surfaces, presumably with low surface energy, which will be discussed later [25,27,28].

High-resolution HAADF-STEM images of a rhombic pore observed in the DC-1400°C sample and a hexagonal pore observed in the AC-1350°C sample, as typical examples, are shown in Fig. 5(a) and (b), respectively. The areas including the pores had the same crystal structures as the original single crystal, which is consistent with SAD patterns shown in Fig. 4(a)–(c). The side planes of the rhombic pore were {111} surfaces, while {001} surfaces appeared in addition to {111} surfaces for the hexagonal pore. As indicated by the white dashed box in Fig. 4(f), the edges of two pores partially overlapped vertically in the STEM thin foil, meaning that the thickness of these pores was less than approximately 60 nm (the thickness of the STEM thin foil). This suggests that these pores had plate-like shapes.

The temperature dependence of the healing ratio for the DC-1250°C, DC-1400°C, and AC-1350°C samples is shown in Fig. 6 (open red and blue symbols). The healing ratio was estimated in two ranges: in the near-surface region (1 μm from the surface, L = 1 μm) and in the interior region (from 1 μm from the surface to 4 μm, L = 3 μm), as shown in the schematic diagram in Fig. 6(a). The healing ratio δ is defined as the sum of the individual pore lengths ΔL_i contained within a length L along the original microcrack:

$$\delta = \frac{L - \sum_{i=1}^{i=m \text{ or } n} \Delta L_i}{L} \times 100\ (\%)$$

In the near-surface region (open circles), the healing ratio increased with increasing sample temperature. This is consistent with the result that the distance from the surface of the pore closest to the surface increased with increasing sample temperature (Fig. 4(d)–(f)). In contrast,

the healing ratio was approximately constant regardless of the sample temperature in the interior region (open squares). In other words, the total volume of the pores in the near-surface region decreased with increasing sample temperature, but that of the pores in the interior region did not change. Previous data obtained for microcrack healing by heat treatment without applying an electric field (black plus signs) and the values reported for zirconia polycrystals by Takahashi et al. [22] (green solid triangles) are also shown in Fig. 6. These data will be discussed later.

Surface topological images of the DC-1400°C and AC-1350°C samples obtained by AFM and the height profiles along the black lines indicated in the AFM images are shown in Fig. 7. In the AFM image of DC-1400°C (Fig. 7(a)), the direction of the DC electric field is indicated by a black block arrow. In the SEM image of DC-1400°C (Fig. 3(c)), the facets on the surface of the DC-1400°C sample mostly formed along the [110] and [$1\bar{1}0$] directions. This facet structure was clearly observed in the AFM topographic image of DC-1400°C (Fig. 7(a)). From the AFM image, the facet structure observed as lines in the SEM image corresponds to the edges of the material uplift from the surface. As shown in the height profile taken along the black line indicated in Fig. 7(a), the material uplift had a saw-like shape with a height of approximately 40 nm (Fig. 7(c)). The height profile showed that the slope of the side wall of this material uplift was asymmetric along the direction of the electric field (from A to B in Fig. 7(a)), with a smaller slope on the front side, as indicated by the arrow in Fig. 7(c). In contrast, the surface of the AC-1350°C sample (Fig. 7(b)) did not show the material uplift observed in the DC-1400°C sample (Fig. 7(a)). In this case, surface step-like structures with heights of approximately 0.2–0.4 nm formed, and some step bunching due to destabilization of the step lines was also observed, as indicated by the black arrows in Fig. 7(b). The large-scale material uplift observed in the DC-1400°C sample is due to drift diffusion by a unidirectional electric field [29, 30].

4. DISCUSSION

4.1. Pore annihilation and field-applied effects for lattice diffusion

After flash healing, the microcrack at the surface was healed with pores remaining in the crystal interior, and the crystal orientation on both sides of the original microcrack was restored to the same orientation relationship as that of the original single crystal. The residual pores were rhombus shaped surrounded by {111} surfaces or hexagon shaped surrounded by {111} and {001} surfaces, in which the upper/lower surfaces of both shapes were possibly surrounded by {110} surfaces. These surrounding inner surfaces are planes with relatively low surface energy [27,28] as discussed previously [25]. The microstructural features observed in the flash-healed single crystals were similar to the results obtained in our previous study on microcrack healing by annealing without an electric field, as shown in Fig. S1 [25]. However, in the case of flash healing, the location of the pore present at the surface-nearest-neighbor position was significantly different from that with no-electric-field thermal healing. In no-electric-field thermal healing, the pore inside the crystal remained close to the surface in the thermal healed sample, in which the distance from the surface to the pore present at the surface-nearest-neighbor position was approximately 40 nm irrespective of the annealing temperature (Fig. S1). In contrast, in the sample after flash healing, the surface-nearest-neighbor pores were located further inside the crystal, as shown in Fig. 4(b) and (c).

The above difference can be inferred to be related to the increase in lattice diffusion during flash treatment as follows. Because the crystallographic orientation relationship is restored to that of the single crystal during flash healing, pore annihilation proceeds by mass diffusion through lattice diffusion. For a pore to be annihilated, the volume contained in the pore must diffuse to the surface through lattice diffusion. The distance from the surface to the pore closest to the surface d is an indication of the amount of mass diffusion through lattice diffusion during healing. As mentioned above, for the DC-1250°C sample, d was approximately 40 nm, which

was comparable to the *d* values of thermal healed samples with no electric field (Fig. S1). In contrast, for the DC-1400°C sample, *d* was approximately 520 nm. This suggests that lattice diffusion increased in the DC-1400°C sample compared with that in the DC-1250°C sample. This increase in lattice diffusion induced by the electric field during flash healing can be considered to be responsible for the increased healing ratio in the near-surface region, as shown in Fig. 6(b) (open circles).

For pores located in the region at a larger distance than *d*, the total volume of the pores hardly changes because it is beyond the distance that pores can be eliminated by lattice diffusion. This was confirmed by the total volume of the pores present in this region hardly changing with the sample temperature, as shown in Fig. 6(b) (open rectangles). In this region, the pore diameter variation due to Ostwald ripening becomes remarkable, in which pores with large diameters become larger, while those with small diameters disappear. This pore size variation due to Ostwald ripening can be observed in the pore size difference by comparing Fig. 4(d) and 4(e), in which the difference in the pore diameter increased for the DC-1400°C sample. The situation in which pores located greater than *d* from the surface are difficult to eliminate should be the same regardless of flash or thermal healing. In fact, the healing ratio in the crystal interior by thermal healing does not change with the sample temperature (plus signs in Fig. 6(b)) [25]. However, the value of *d* will increase if the temperature and time are sufficient to promote lattice diffusion even in thermal healing. Similarly, *d* is expected to increase further also in flash healing.

According to Gupta [10,11], in the early stage of microcrack healing, there is a progressive increase in the contact area between the crack inner surfaces owing to surface diffusion. As shown in Fig. 7, the DC-1400°C sample showed surface material uplift with a height of approximately 40 nm and the characteristic facet structure. This surface material uplift is considered to be due to drift diffusion induced by the DC electric field [29,30]. In contrast, the

AC-1350°C sample did not show the effect of drift diffusion that occurred during application of the DC electric field, and no facet structure was observed on the crystal surface. This difference in the surface morphologies under DC and AC electric fields indicates a difference in surface diffusion, which is expected to affect the early stage of healing. However, from the healing ratios (Fig. 6), the healing ratio in the AC-1350°C sample was close to the sample temperature dependence of the healing ratios of the DC-1250°C and DC-1400°C samples. This means that the contribution of surface diffusion to the early stages of microcrack healing is possibly not significant for zirconia single crystals.

4.2. Role of grain boundaries during flash healing

As mentioned above, once a pore is isolated and confined within the crystal interior that has been restored to the single crystal orientation relationship during microcrack healing, a subsequent decrease in the total volume of the pores is very unlikely to occur. To increase the annihilation rate, more effective diffusion paths are necessary, and grain boundaries act as effective diffusion paths for this purpose. Morita and co-workers [12, 22] systematically investigated the flash-healing behavior of microcracks in zirconia polycrystals. The results of flash healing of microcracks in zirconia polycrystals with different grain sizes, that were flash treated with DC electric field, are shown as green solid triangles in Fig. 6 [22]. In the case of a zirconia polycrystal with a grain size of approximately 0.8 μm, the microcrack was completely healed in 10 min by DC flash healing at a sample temperature of 1230 °C. Healing of microcracks in the zirconia polycrystals was confirmed to be completed not only on the surface, but also in the interior. This healing ratio is much higher than those obtained for zirconia single crystals. This means that grain boundaries allow healing to rapidly proceed. The healing ratio significantly decreased as the grain size of the zirconia polycrystal increased. This is probably because a larger distance must be travelled via lattice diffusion for larger grain size. This

situation is similar to the discussion of the positional relationship of the surface-nearest pore to the surface described in Section 4.1. In other words, the reason why the healing ratio decreases with increasing grain size is probably the existence of grain boundaries located at a distance greater than the distance at which pores can be annihilated. Grain boundaries act as effective annihilation sites for pores contained in grain interiors [31]. Nambu et al. [32] observed similar annihilation of pores in the presence of grain boundaries by flash bonding. Thus, the presence of grain boundaries may play an important role in promoting flash repair.

5. Conclusions

Microstructural observations, mainly by STEM, have been performed for flash-healed microcracks formed by a Vickers indentation on the (001) surface of cubic zirconia single crystals. The following results were obtained.

(1) The microcracks on the (001) plane of the single crystal due to Vickers indentation formed along the [110] and [$1\bar{1}0$] directions with an average half-length from the center of the indent of approximately 22.5 μm.

(2) Surface observation by SEM revealed that the surface area where the microcracks existed was healed by flash healing for 10 min at 100 V/cm with limit currents of 150 and 350 mA/cm^2 for a DC electric field, and at 100 V/cm with a limit of 350 mA/cm^2 for an AC electric field.

(3) Internal observation by STEM revealed that the crystallographic orientation of the crystal areas containing a closed microcrack completely returned to that of the original single crystal, although a row of plate-like rhombic and hexagonal pores remained along the original microcrack location. Elimination of these pores can be considered to proceed by lattice diffusion.

(4) The healing ratio of the near-surface region by flash healing was higher than that by thermal healing without an electric field. Furthermore, the location of the pore closest to the surface was further inside the crystal for flash healing than for thermal healing. These results suggest that lattice diffusion is enhanced by flash healing.

(5) Pores located in the interior of the crystal beyond the distance that can be eliminated by lattice diffusion are difficult to eliminate. The presence of grain boundaries with fast diffusion paths beyond the distance that can be eliminated by flash treatment is effective to eliminate these pores.

Acknowledgments

This work was financially supported by CREST (JPMJCR1996) from the Japan Science and Technology Agency, and JSPS KAKENHI (Grant Number JP19H05788).

References

1) A. G. Evans, Perspective on the development of high-toughness ceramics, J. Am. Ceram. Soc., 73 (1990) 187-206. https://doi:10.1111/j.1151-2916.1990.tb06493.x

2) R. C. Garvie, R.H. Hannink, Ceramic steel?, Nature, 258 (1975) 703–704. https://doi:10.1038/258703a0.

3) J. Wang, R. Stevens, Zirconia-toughened alumina (ZTA) ceramics, J. Mater. Sci., 24 (1989) 3421–3440. https://doi:10.1007/BF02385721.

4) H. Siddiqui, K. Pickering, M. Mucalo, A review on the use of hydroxyapatite-carbonaceous structure composites in bone replacement materials for strengthening purposes, Materials, 11 (2018) 1813. https://doi:10.3390/ma11101813.

5) S. Gali, K.R. Kumar, B.V.S. Murthy, B. Basu, Zirconia toughened mica glass ceramics for dental restorations, Dental Mater., 34 (2018) e36–e45. https://doi:10.1016/j.dental.2018.01.009.

6) I. Hammood, G. Barber, B. Wang, A review of some of experimental and numerical studies of self-crack-healing in ceramics, Int. J. Ceram. Eng. Sci., 2 (2020) 274–291. https://doi.org/10.1002/ces2.10071

7) F. Tavangarian, D. Hui, G. Li, Crack-healing in ceramics, Compos. B. Eng., 144 (2018) 56–87. https://doi.org/10.1016/j.compositesb.2018.02.025

8) FF. Lange, KC Radford, Healing of surface cracks in polycrystalline Al_2O_3, J. Am. Ceram. Soc., 53 (1970) 420–421. https://doi.org/10.1111/j.1151-2916.1970.tb12148.x

9) FF. Lange, TK. Gupta TK. Crack healing by heat treatment. J. Am. Ceram. Soc., 53 (1970) 54–55. https://doi.org/10.1111/j.1151-2916.1970.tb12002.x

10) T.K. Gupta, Instability of cylindrical voids in alumina, J. Am. Ceram. Soc., 61 (1978) 191-195. https://doi.org/10.1111/j.1151-2916.1978.tb09276.x

11) T.K. Gupta, Crack healing and strengthening of thermally shocked alumina, J. Am. Ceram. Soc., 59 (1976) 259-262. https://doi.org/10.1111/j.1151-2916.1976.tb10949.x

12) K. Morita, F. Naito, D. Terada, Microcrack healing in zirconia ceramics under a DC electric field/current, J. Eur. Ceram. Soc., 41 (2021) 282–289. https://doi.org/10.1016/j.jeurceramsoc.2021.09.044

13) J. Dong, V. M. Sglavo, M. Kermani, X. Su, T. Saunders, C. Hu, S. Grasso, Athermal electric field effects in flash sintered zirconia, Adv. Appl. Ceram., 120 (2021) 193-201. https://doi.org/10.1080/17436753.2021.1919361

14) M. Cologna, B. Rashkova, R. Raj, Flash sintering of nanograin zirconia in <5s at 850◦C, J. Am. Ceram. Soc., 93 (2010) 3556–3559. https://doi.org/10.1111/j.1551-2916.2010.04089.x

15) M. Yu, S. Grasso, R. Mckinnon, T. Saunders, M.J. Reece, Review of flash sintering: materials, mechanisms and modelling, Adv. Appl. Ceram., 116 (2017) 24–60. https://doi.org/10.1080/17436753.2016.1251051

16) O. Guillon, R.A. De Souza, T.P. Mishra, W. Rheinheimer, Electric‐field‐assisted processing of ceramics: nonthermal effects and related mechanisms, MRS Bull., 46 (2021) 52–58. https://doi.org/10.1557/s43577-020-00008-w

17) Y. Ishino, K. Taguchi, M. Koike, T. Tokunaga, T. Yamamoto, Shrinkage rate control during a flash state by current-ramping for 3 mol% Y_2O_3-doped ZrO_2 polycrystals, J. Am. Ceram. Soc., 104 (2021) 4960–4967. https://doi.org/10.1111/jace.17912

18) H. Yoshida, Y. Sakka, T. Yamamoto, JM. Lebrun, R. Raj, Densification behavior and microstructural development in undoped yttria prepared by flash-sintering, J. Euro. Ceram. Soc., 34 (2014) 991-1000. https://10.1016/j.jeurceramsoc.2013.10.031

19) R.I. Todd, E.Z. Solvas, R.S. Bonilla, T. Sneddon, P.R. Wilshaw, Electrical characteristics of flash sintering: thermal runaway of Joule heating, J. Euro. Ceram. Soc., 35 (2015) 1865-1877. https://10.1016/j.jeurceramsoc.2014.12.022.

20) K. Ren, QK. Wang, YL. Lian, YG. Wang, Densification kinetics of flash sintered 3mol% Y_2O_3 stabilized zirconia, J. Alloys Compd., 747 (2018) 1073-1077.

https://10.1016/j.jallcom.2018.02.308

21) M. Cologna, A.L. Prette, R. Raj, Flash-sintering of cubic yttria-stabilized zirconia at 750 ℃ for possible use in SOFC manufacturing, J. Am. Ceram. Soc., 94 (2011) 316–319.

22) S. Takahashi, K. Morita, K. Nambu, D. Terada, K. Kobayashi, T. Tokunaga, T. Yamamoto, Effect of initial grain size on crack healing behavior under DC electric field of zirconia (8Y-CSZ) ceramic, Adv. Eng. Mater., (2023) 2201807. https://10.1002/adem.202201807.

23) A. Pajares, F. Guiberteau, A. D-Rodriguez, A. H. Heuer, Indentation-induced cracks and the toughness anisotropy of 9.4-mol%-yttria-stabilized cubic zirconia single crystals, J. Am. Ceram. Soc., 74 (1991) 859-862. https://doi.org/10.1111/j.1151-2916.1991.tb06941.x

24) N. Morisaki, H. Yoshida, K. Matsui, T. Tokunaga, K. Sasaki, T. Yamamoto, Synthesis of zirconium oxynitride in air under DC electric fields, Appl. Phys. Lett., 109 (2016) 083104. https://doi.org/10.1063/1.4961624

25) S. Kayukawa, Y Katsuyama, A. Kodaira, T. Tokunaga, K. Morita, A. Nakamura, K. Higuchi, T. Yamamoto, Microcrack healing in single-crystal cubic zirconia by thermal annealing, J. Euro. Ceram. Soc., 43 (2023) 1078–1086. https://doi.org/10.1016/j.jeurceramsoc.2022.10.065.

26) W.Ji, B. Parker, S.Falco, J.Y. Zhang, Z.Y. Fu, R.I.Todd, Ultra-fast firing: Effect of heating rate on sintering of 3YSZ, with and without an electric field, J. Euro. Ceram. Soc., 37 (2017) 2547-2551. http://dx.doi.org/10.1016/j.jeurceramsoc.2017.0.

27) A. Christensen, E.A. Carter, First-principles study of the surfaces of zirconia, Phys. Rev. B. 58 (1998) 8050–8064. https://doi.org/10.1103/PhysRevB.58.8050

28) G. Ballabio, M. Bernasconi, F. Pietrucci, S. Serra, Ab initio study of yttria-stabilized cubic zirconia surfaces, Phys. Rev. B., 70 (2004) 075417. https://doi.org/10.1103/PhysRevB.70.075417

29) Y. Homma, N. Aizawa, Electric-current-induced step bunching on Si (111), Phys. Rev. B., 62 (2000) 8323-8329. https://doi.org/10.1103/PhysRevB.62.8323

30) E. E. Rodyakina, S. S. Kosolobova, A.V. Latyshev, Drift of adatoms on the (111) silicon surface under electromigration conditions, JETP Lett., 94 (2011) 147–151. https://doi.org/10.1134/S0021364011140128

31) J.E. Burke, Role of grain boundaries in sintering, J. Am. Ceram. Soc., 40 (1957) 80–85. https://doi.org/10.1111/j.1151-2916.1957.tb12580.x

32) K. Nambu, T. Kitaoka, K. Morita, K. Soga, T. Tokunaga, T. Yamamoto, H. Masuda, H. Yoshida, Flash self-joining of Y-TZP ceramics assisted with an AC electric field, J. Am. Ceram. Soc., 106 (2023) 2073-2082. https://doi.org/10.1111/jace.18889.

FIGURE 1

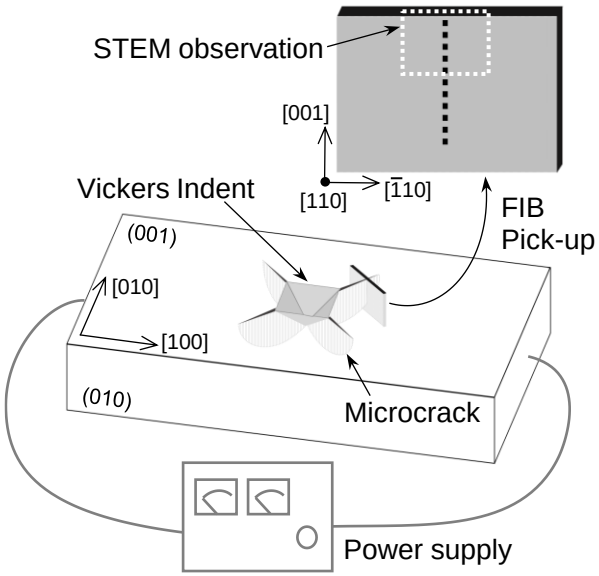

FIGURE 1

Schematic illustration of the sample setup for flash healing and FIB pick-up for STEM thin foil preparation with the crystallographic orientation index. The edges of Vickers indent are parallel to (010) and (100) of single crystal.

FIGURE 2

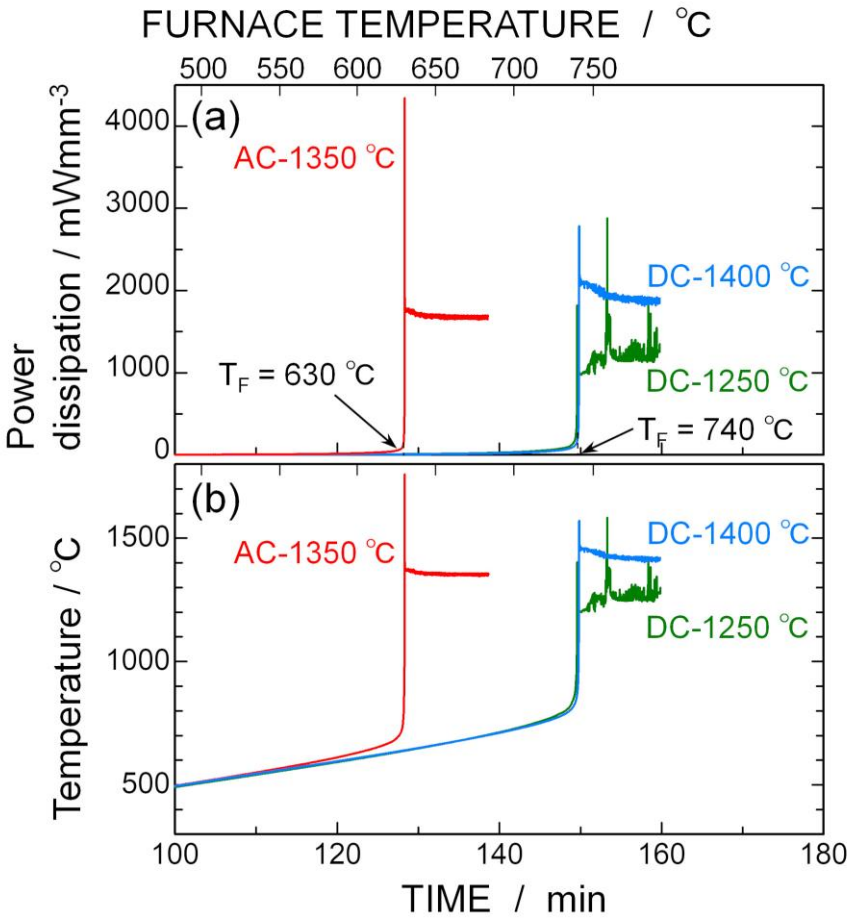

FIGURE 2

Changes of the (a) power dissipation and (b) sample temperature with the process time. The sample temperatures were calculated using an equation based on a black-body radiation model [26]. T_F is the flash temperature. Furnace temperature is indicated at an upper horizontal axis of (a) for reference. In respective flash treatment, when the furnace temperature reaches the respective flash temperature, the furnace temperature ramp is stopped and is maintained at a constant temperature thereafter.

FIGURE 3

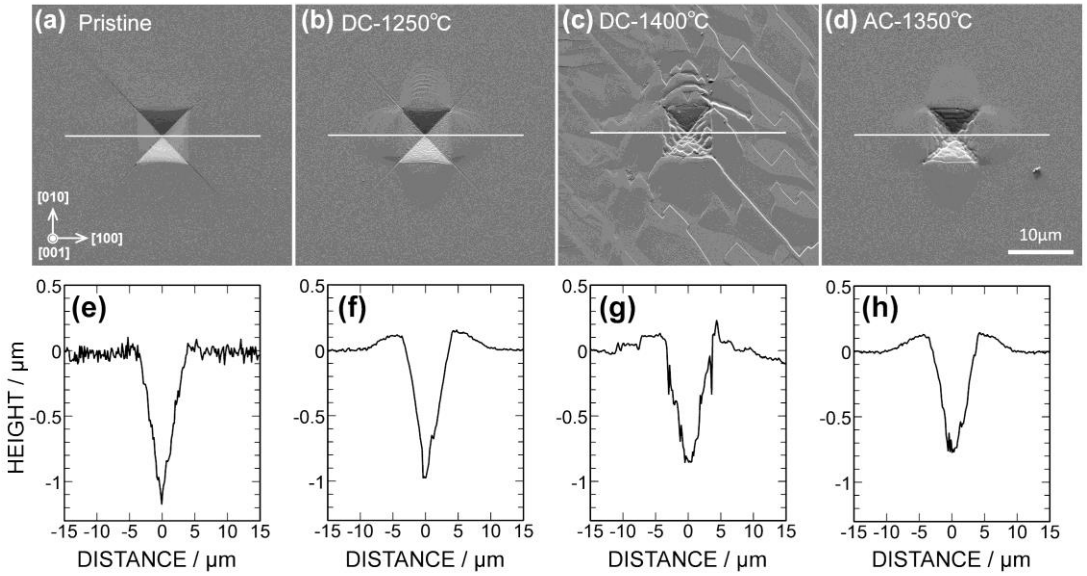

FIGURE 3

(a)–(d) SEM images of the surface morphologies and (e)–(h) height profiles as a function of the distance: (a) and (e) pristine sample, (b) and (f) DC-1250℃ sample, (c) and (g) DC-1400℃ sample, and (d) and (h) AC-1350℃ sample. The height profiles in (e)–(h) were taken along the white lines indicated in the respective SEM images. The label of the vertical axis of the height profiles is shown in (e). The SEM image and height profile of the pristine sample in (a) and (e) were taken from Ref. 25.

FIGURE 4

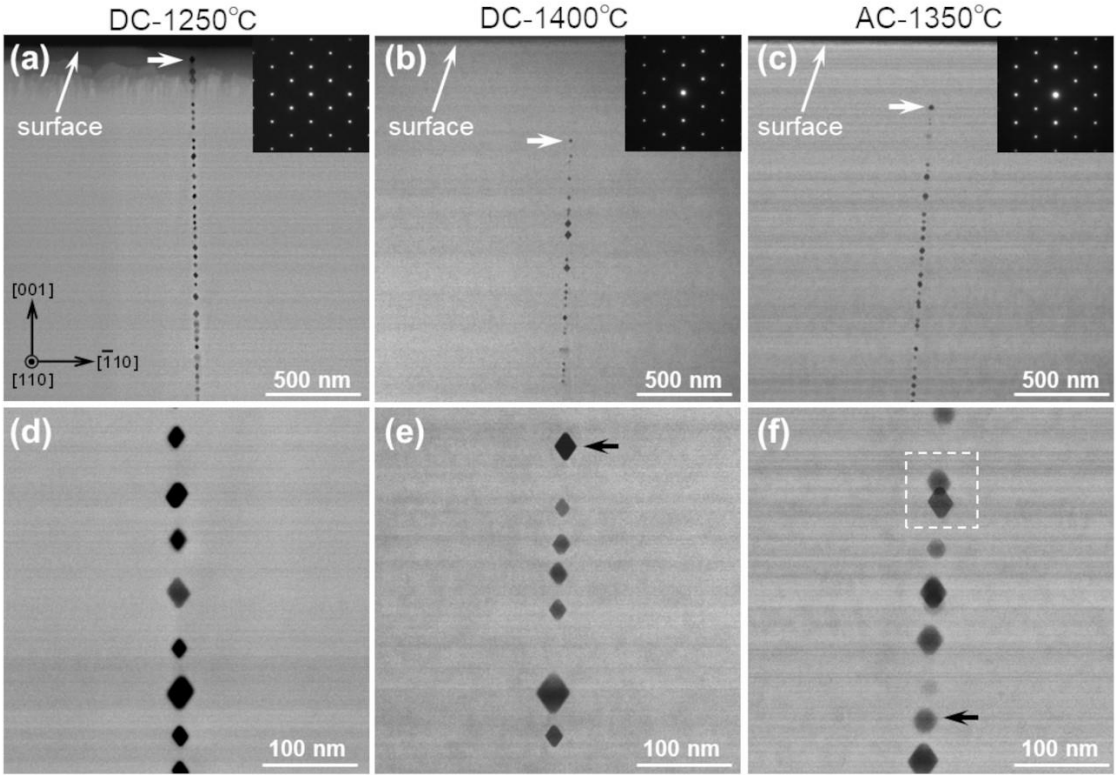

FIGURE 4

HAADF-STEM images of the (a) and (d) DC-1250 ℃, (b) and (e) DC-1400 ℃, and (c) and (f) AC-1350 ℃ samples. The horizontal white arrows in (a)–(c) indicate the pores closest to the surfaces. The inserts show the SAD patterns of the areas including both sides of the microcracks (rows of pores).

FIGURE 5

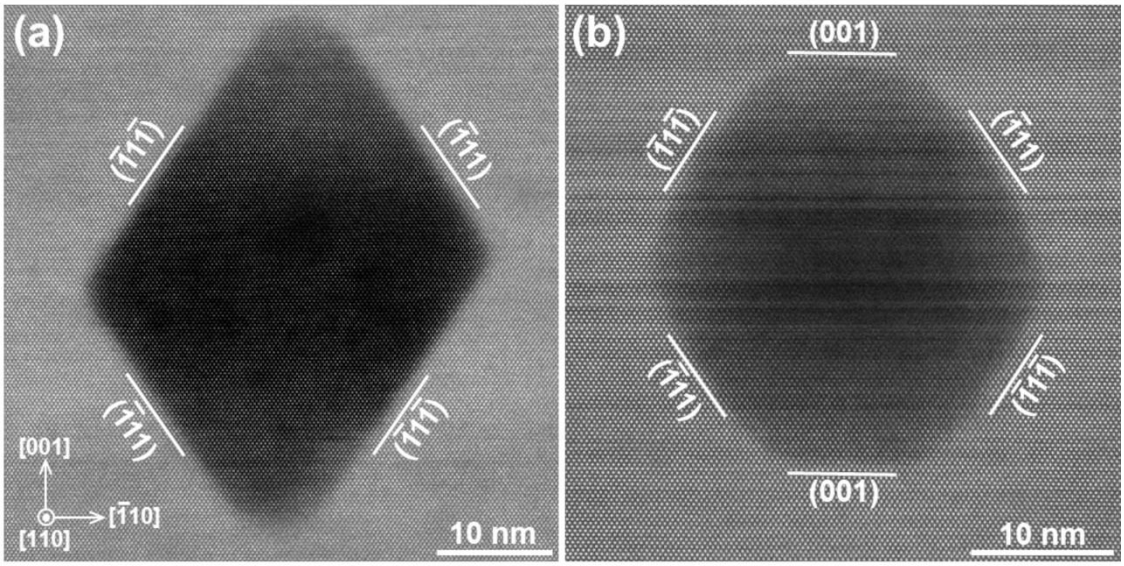

FIGURE 5

High resolution HAADF-STEM images of a typical rhombic pore in the DC-1400 ℃ sample and (b) a hexagonal pore in the AC-1350 ℃ sample. It is noted that scales of respective STEM images are different.

FIGURE 6

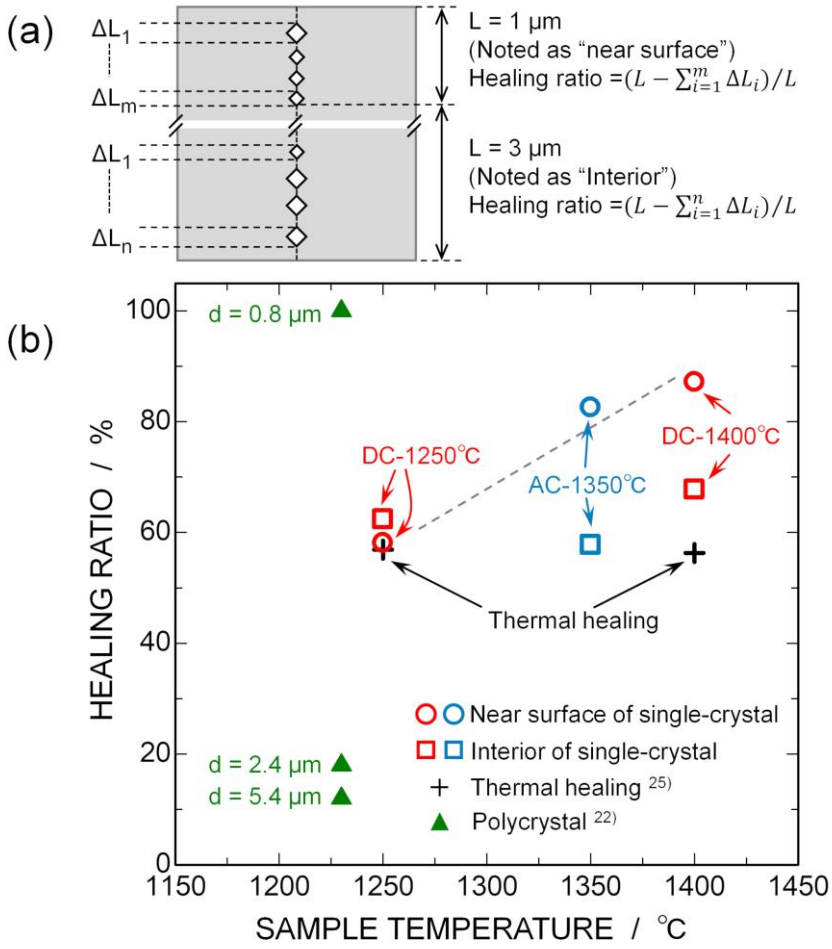

FIGURE 6

(a) Schematic illustration showing how the healing ratio was calculated. (b) Plot of the healing ratio against the sample temperature: ○, ○, near-surface region of the zirconia single crystals after flash healing; □, □, inside the zirconia single crystals after flash healing; +, after thermal healing of zirconia single crystals [25]; ▲, after flash healing of zirconia polycrystals [22]. The average grain sizes, *d*, of the polycrystals are indicated beside the ▲ symbols.

FIGURE 7

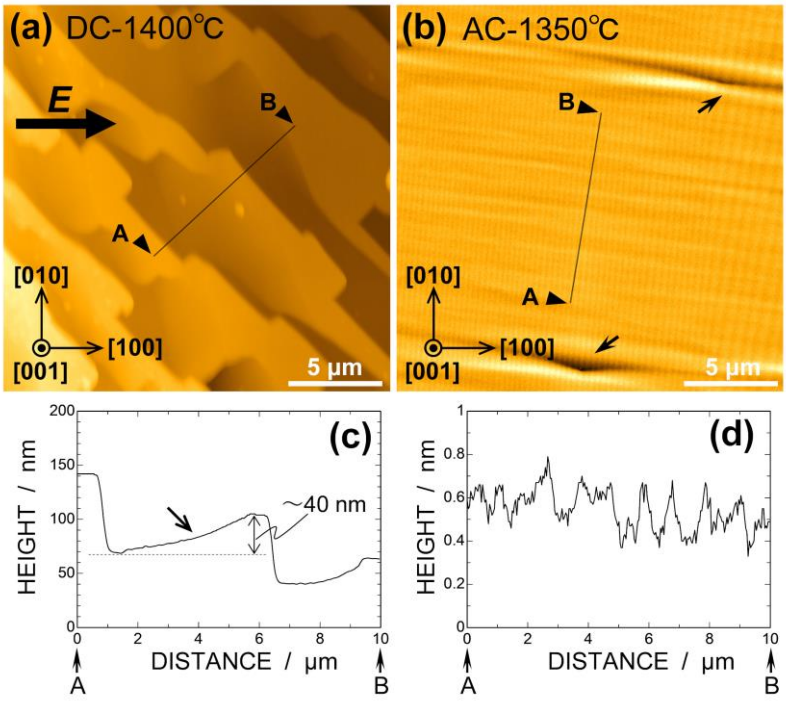

FIGURE 7

AFM topological images and height profiles along the black lines shown in the AFM images: (a) and (c) the DC-1400 ℃ sample, and (b) and (d) the AC-1350 ℃ sample. Note that the scales of the vertical axes of the height profiles are different.

Supplementary figure

FIGURE S1

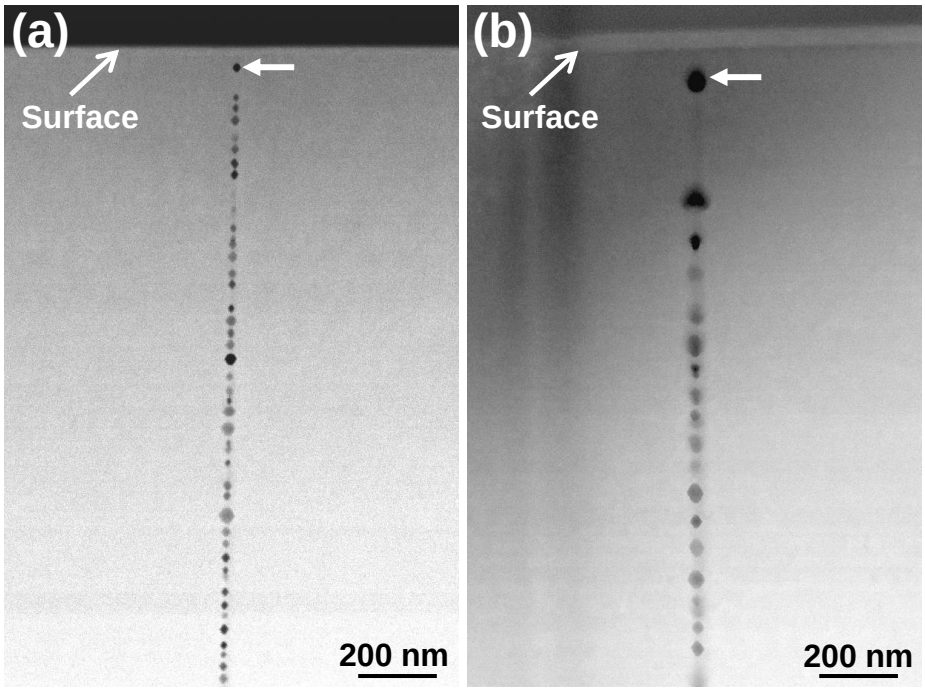

FIGURE S1

HAADF images taken from thermally healed cubic zirconia single crystals with Vickers indents that were annealed at (a) 1250 ℃, and (b) 1400 ℃. The block arrows show the pores closest to surfaces. These images were taken from Ref. 25.